Investigation of Al-Zn-Zr and Al-Zn-Ni Alloys for High Electrical Conductivity and Strength Application

Oladeji Fadayomi, Rachel Clark, Violet Thole, Paul G. Sanders, Gregory M. Odegard

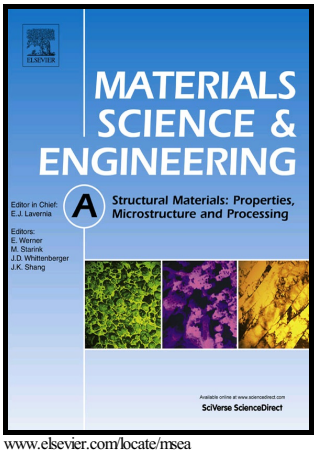

www.elsevier.com/locate/msea

PII: S0921-5093(18)31637-X
DOI: https://doi.org/10.1016/j.msea.2018.11.111
Reference: MSA37231

To appear in: *Materials Science & Engineering A*

Received date: 17 September 2018
Revised date: 21 November 2018
Accepted date: 22 November 2018

Cite this article as: Oladeji Fadayomi, Rachel Clark, Violet Thole, Paul G. Sanders and Gregory M. Odegard, Investigation of Al-Zn-Zr and Al-Zn-Ni Alloys for High Electrical Conductivity and Strength Application, *Materials Science & Engineering A,* https://doi.org/10.1016/j.msea.2018.11.111

Investigation of Al-Zn-Zr and Al-Zn-Ni Alloys for High Electrical Conductivity and Strength Application

Oladeji Fadayomi, Rachel Clark, Violet Thole, Paul G. Sanders, Gregory M. Odegard

Department of Materials Science and Engineering, Michigan Technological University, 49931 USA

Abstract

Al-Zn-TM (TM=Transition metals) alloys are developed with an integrated computational material engineering (ICME) strategy. Al-Zn-Ni and Al-Zn-Zr are determined to have promising electrical conductivities via a series of *ab initio* density functional theory (DFT) simulations assessing combinations of Al-TM and Al-Zn-TM. The computed enthalpies of formation are used to identify the zero-temperature equilibrium precipitate phase in both alloys with increasing levels of Zn content, with a particular focus of finding Zn content levels that result in a precipitate $L1_2$ structure. The corresponding microhardness and electrical conductivity measurements of both alloys are evaluated. Transmission Electron Microscopy (TEM) is used to examine the morphology of the $Al_{3-x}Zn_xNi$ and $Al_{3-x}Zn_xZr$ precipitates formed in the respective alloys and their structures were confirmed as $L1_2$ by selected area electron diffraction (SAED). Through qualitative chemical analysis, it is demonstrated that Ni and Zr are not present in the matrix but are completely used up in forming the respective precipitate phases in both alloys.

Keywords: Aluminum alloys; Precipitation; Age hardening; Al-Zn-Ni; Al-Zn-Zr

1. Introduction

The Integrated Computational Materials Engineering (ICME) approach involves the use of computational simulation tools to facilitate the materials development process for targeted high strength and electrical conductivity engineering applications[1], thus reducing the number of design iterations and overall development time and cost. The ICME approach is well suited for the development of new aluminum alloy systems because of the presence of well-defined metrics (e.g. electrical conductivity and energy of formation) and a corresponding structure-property simulation tool for this purpose. For the ICME development of new metallic alloys, Density Functional Theory (DFT)[2] is a powerful computational tool for predicting stable crystal structures and estimating electrical conductivities for multi-element alloy systems. DFT has been used extensively for predicting structural, physical, and chemical properties of aluminum alloys and intermetallic compounds. Such properties include elastic constants[3,4,5], lattice parameters[6], stable microstructures, and density of states[7,8,9]. As the initial step in the ICME process, a broad range of Al alloys was selected for exploration of electrical conductivity and subsequent prediction of equilibrium precipitate phase structure.

Precipitation strengthening is one of the most effective mechanisms for enhancing alloy strength. For improved retention of precipitation hardened Al alloy strength, transition metal (TM) elements were specifically selected as solutes, because of their low rate of diffusivity and

favorable solvus line with high solubility at solutionizing temperatures and low solubility at aging temperatures. The low rate of TM diffusivity in aluminum reduces the rate of precipitate coarsening, thus retaining the alloy strength at elevated service temperatures for longer periods of time. The low solubility at aging temperatures increases the precipitate volume fraction and corresponding precipitation strengthening because a majority of the solute atoms precipitate out of solid solution during aging. Low concentrations and solid solubility of alloying elements, especially in solution, are required to minimize their negative impact on the electrical conductivity. Another important benefit of using some transition metals includes resistance to corrosion[10].

Since aluminum has an fcc crystal structure, it is desirable to form precipitates with $L1_2$ crystal structure to minimize lattice mismatch and enhance precipitate/matrix lattice coherency. Coherency strains due to the minimal lattice mismatch is responsible for improved creep resistance and alloy strength through obstruction of dislocation motion by the strain fields surrounding the coherent precipitates[11]. A large lattice mismatch (observed in incoherent and semi-coherent precipitates) can be a driving force for precipitate coarsening. Therefore, it is expected that coherent $L1_2$ precipitates provide greater strengthening phases than precipitates of other crystal structures. Of all binary Al-TM systems, only Al_3Sc trialuminide has a thermodynamically stable $L1_2$ structure, although several studies have shown that metastable $L1_2$-Al_3Zr precipitate structures form in Al-Zr alloys during aging. However, some of these $L1_2$ precipitates transform back to their equilibrium $D0_{23}$ structure at high temperatures (> 475 ℃)[12,13]. Precipitates formed in binary Al-Ni alloys have a stable orthorhombic $D0_{11}$–Al_3Ni phase[14], which is incoherent with the α-Al matrix. Thus, there is a need for precipitate phase transformation from $D0_{11} \rightarrow L1_2$.

Most TMs have a very low solid solubility limit ($< 1\ at.\%$) in the α-Al matrix, which limits the volume fractions of the precipitate formed in binary Al-TM alloys to $\phi < 1\ vol\ \%$ from aging, and their corresponding strengthening from precipitation hardening[11]. Thus, there is a need to develop ternary Al-TM_1-TM_2 alloys with stable $L1_2$ precipitate phases and increased precipitate volume fractions. Several studies of Al-Zr-Ti and Al-Zr-Sc ternary alloys have shown improved $L1_2$ precipitate volume fractions and corresponding microhardness values relative to Al-Zr, but their electrical conductivities are severely impacted[12,13]. For instance, Knipling determined the electrical conductivities of Al-0.1Zr-0.1Ti and Al-0.1Zr-0.1Sc (at.%) as 26.6 and 26.4 MS/m at as-cast and 29.2 and 32.8 MS/m at peak conditions, respectively[12,30].

To form a suitable ternary aluminum alloy with high electrical conductivity, a natural choice of a TM element is Zn. As shown in Figure 1, Zn has a minimal impact on electrical conductivity of Al, relative to other elements. However, it is generally more soluble in aluminum than other TM elements, hence, most of the added Zn remains in solid solution during the aging process[11]. It has been shown that the addition of Zn to aluminum results in minimal improvement of tensile strength through solid solution strengthening[11]. Thus, it follows that binary Al-Zn alloys are not suitable for achieving both high conductivity and strength. When in solid solution, solutes have significantly more negative impact on the electrical conductivity of the alloys (Figure 1) than when out of solution[10]. Taking advantage of Zn solute's minimal impact on the electrical conductivity of Al, when in or out of solution, ternary Al-Zn-TM alloys with improved strength could therefore be developed, while still maintaining high electrical conductivity of the alloys[15].

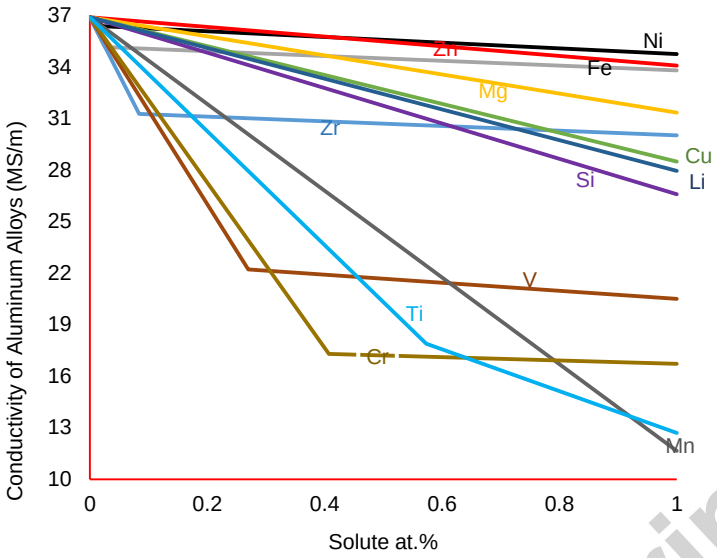

Figure 1. Experimental values of the electrical conductivity drop due to addition of 0-1 wt.% of each TM solute atom in binary Al-TM alloys. Adapted from Hatch at room temperature 20°C[10]. The change in slope occurs at the solvus line and corresponds to the composition beyond which excess solute precipitates out of solution.

Studies have also shown that adding Zn to certain binary Al-TM alloys to form $L1_2$ ternary Al-Zn-TM compounds are possible. The elements known to stabilize the ternary $L1_2$ crystal structure with respect to non-cubic $D0_{22}$, $D0_{23}$ and $D0_{11}$ all have atomic radii smaller than aluminum and contribute to the reduction of the c/a ratio of the $D0_{22}$, $D0_{23}$ and $D0_{11}$ phases[16,17,18] or the number of d-shell electrons[16,17]. For these reasons, the addition of Zn could be effective for transforming the non-cubic precipitate structures of Al_3Ni to $L1_2$. According to Fine et al.[15], the use of ab-initio modeling predicts that adding Zn to Al_3Zr improves the stability of metastable $L1_2$ precipitate phase. They verified this via qualitative comparison of EDX data from the matrix and precipitate.

The objective of this study was to use ICME to facilitate the design, fabrication, and testing of new aluminum alloy systems for high electrical conductivity applications, with improved mechanical properties, such as microhardness and yield strength. One application for these alloys is high-voltage electrical power transmission cables. DFT simulations were used to efficiently screen candidate alloy systems for subsequent experimental testing. Based on DFT results, Al-Zn-Zr and Al-Zn-Ni alloy systems were selected for experimental analysis because of their relatively high electrical conductivity and ability to form stable $L1_2$ precipitate phase required for improved alloy strengthening. In this paper, the computational effort is first described, followed by the experimental fabrication and characterization.

2. Computational modeling

This section describes the computational modeling methods and results that were used to efficiently down-select Al-Zn-Zr and Al-Zn-Ni as alloy candidates with optimal properties (electrical conductivity and precipitate phase stability).

2.1. Method of electrical conductivity prediction

The DFT approach was selected for this study because it efficiently provides a first-order prediction of the electrical conductivity and zero-temperature stability of the $L1_2$ precipitate phase for different alloy systems. For the DFT simulations, the generalized gradient approximation (GGA) with Perdew-Burke-Ernzerhof (PBE) functional was used as implemented in the plane-wave Vienna Ab-initio Simulation Package (VASP)[19]. Specifically, the pseudo-potential utilized for the simulation of each binary and ternary alloy system was a concatenation of the pseudo-potentials of the individual elements present in the specific alloy system simulated. These pseudo-potentials were selected from the PAW-PBE_52 category and included Zn_pv_GW, Zr_sv_GW, Ni_sv_GW and Al_sv_GW. For all other transition elements, the TM_sv_GW pseudo-potential was selected, because it generated physical properties (e.g. lattice parameters) that were consistent with experiment data.

In general, the electrical conductivity of metals is affected by the crystal structure, the presence of impurities, and temperature (which causes atomic vibrations that disrupt the transport and energetics of electrons near the Fermi surface). Although all these factors can be simulated using large ab initio Molecular Dynamics simulations (a series of DFT simulations that include thermal motion) and the Kubo-Greenwood formula[20,21], this approach can be prohibitively time consuming for material screening efforts such as this. The electrical conductivity of metal alloys is also dependent on whether the alloying elements are in or out of solution (precipitation). The negative impact of alloying elements in solid solution on electrical conductivity is greater than when out of solid solution as secondary phase precipitates[10].

A more efficient approach is to use the semi-classical method[22], which predicts the electrical conductivity with a single DFT simulation at 0 K. Although this approach does not consider the influence of thermal fluctuations on the scattering of electrons or precipitation of secondary phases from solid solution, it does consider the density of state (DOS) predictions and the influence of temperature on the smoothed Fourier interpolation of the band. The semi-classical approach calculates the electrical conductivity tensor using the Boltzmann transport equations

$$\sigma_{ij}(\varepsilon) = \frac{1}{N}\sum_{i,k} e^2 \tau_{i,k}\, v_\alpha(i,k)\left(-\frac{\delta(\varepsilon-\varepsilon_{i,k})}{d\varepsilon}\right) \quad (1)$$

$$\sigma_{ij}(T,\mu) = \int \sigma_{ij}(\varepsilon)\left(-\frac{\delta P(T,\varepsilon)}{\delta\varepsilon}\right) d\varepsilon \quad (2)$$

where $P(T,\varepsilon)$ is the Fermi-Dirac distribution, i and j are tensor indices, e is the electron charge, N is the number of k-points sampled, v is the band velocity, and τ is the relaxation time. VASP assumes a constant τ for charge carriers, which can be set using the RTIME command (in femtoseconds). The first equation is energy-dependent, while the second is a function of temperature T and chemical potential μ[24]. In VASP, the chemical potential is considered to be the same as the Fermi level.

The number of states sampled with Equation (1) is dependent on the concentration of electrons in the conduction band n_c. The density of states is a function $\rho_{energy}(\varepsilon)$ that when multiplied by an interval of energy $d\varepsilon$ between energy states, ε and $\varepsilon + d\varepsilon$, provides the total concentration of the available states. It however does not provide any information about the number of states occupied by charge carriers (e.g. electrons). Therefore, the probability that an electron resides at a given energy is denoted by $P(\varepsilon)$, while the concentration of electrons at a given energy ε is given as[23]:

$$n_e(\varepsilon) = P(\varepsilon)\rho_{energy}(\varepsilon)d\varepsilon \qquad (3)$$

where $P(\varepsilon)$ is the Fermi-Dirac distribution and $P(\varepsilon)\rho_{energy}(\varepsilon)$ implies that most of the electrons reside near the conduction band edge. Hence, the total concentration of electrons in the conduction band is given by:

$$n_c = \int_{\varepsilon_C}^{\infty} P(\varepsilon)\rho_{energy}(\varepsilon)d\varepsilon \qquad (4)$$

ε_C is the starting energy of the conduction band. This method has been successfully used previously for predictions of electrical conductivity[24,25,26,27].

It is important to note that the electrical conductivity predictions using this approach are only helpful for studying relative differences in the conductivity between different systems, not for predicting the absolute magnitude of conductivity for comparison with experiments. As described above, this approach neglects the effects of electron scattering due to thermal fluctuations. Also, because of the computational demands of DFT simulations, only relatively small systems can be efficiently simulated (< 100 atoms). Thus, only single crystals can be simulated, and the effects of precipitates are generally neglected. Therefore, the absolute predictions of electrical conductivity using this approach are not meaningful, only the relative differences in conductivity due to atomic structural changes are helpful.

2.2. Effect of spatial arrangement on electrical conductivity

Before DFT simulations were performed to predict the electrical conductivity trends of Al-Zn-TM combinations, a sub-set of alloy supercells were modeled to establish the dependence of the placement of alloying elements within the supercell on electrical conductivity. The face-centered cubic (FCC) supercells listed in Table 1 were constructed, each consisting of 108 atoms (3×3×3 unit cells). For each alloy system (except pure Al) two supercells were constructed, one with clustered alloying elements, and another with dispersed alloying elements. For example, Figure 2 shows the cluster and disperse supercells for the $Al_{106}ZnZr$ alloy system. For the cluster configuration, the two atoms of the alloying elements were placed at the face center and corner lattice positions in a single FCC unit cell within the supercell (first neighbor positions). In the disperse configuration, an atom of the first alloying element was placed at the eight (8) corners of the super cell (amounting to 1 solute atom/supercell), while an atom of the second alloying element was placed within the supercell. These models represent ~0.926 at. % of each solute atom. This composition is well above practical solid solubility limit of most transition metals (Figure 1) which have solubility limits that are $\ll 1\ at.\%$ in aluminum. However, larger DFT supercells would need to be constructed to get lower concentration levels of solute atoms, which

would become prohibitively time-consuming considering the large number of systems considered in this study.

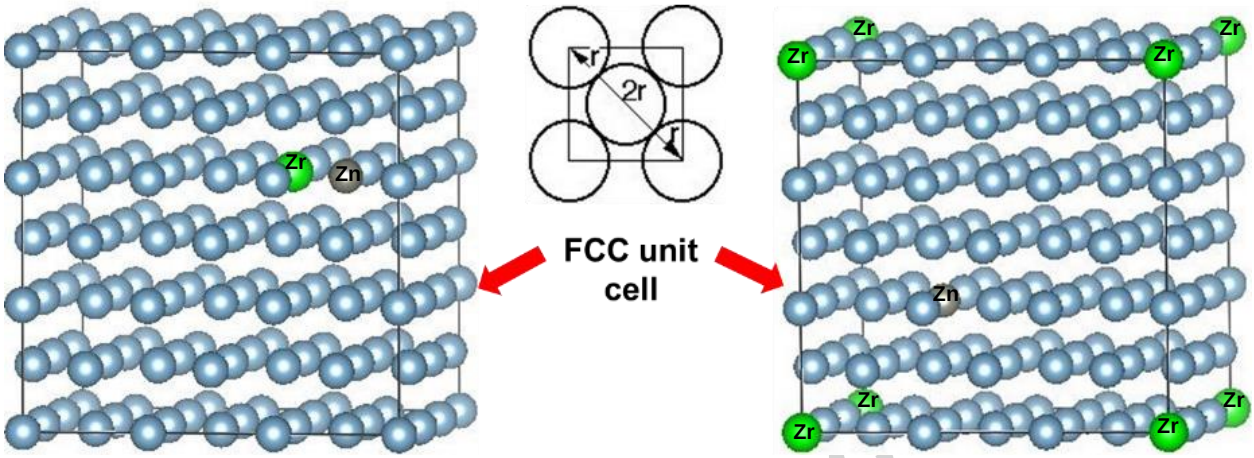

Figure 2. Clustered (left) vs disperse (right) supercell structures, consisting of aluminum (Blue atoms), Zn (grey atoms) and Zr (green atoms). Each supercell has a size of 3x3x3 FCC unit cells consisting of 108 atoms.

The electrical conductivity (MS/m) tensor was calculated for each alloy system using the VASP command "LOPTICS = .TRUE.". The Methfessel-Paxton method (of order 1) was used for smoothing of the energy bands. The energy cutoff was set to 550 eV, while the Brillouin zone sampling was performed using 6 x 6 x 6 k-point Γ-centered Monkhorst-Pack mesh. Table 1 shows the predicted electrical conductivities with respect to the Al_{108} system for each of the alloy system in the cluster and disperse configurations. In the table, the electrical conductivity of pure Al was normalized to 1. Electrical conductivities of the ternary alloy systems were also normalized as a fraction of the electrical conductivity of pure Al. Hence, σ_C and σ_D are the normalized values (with no units). The lattice constants included in the Table 1 are the lengths of the simulation cells after relaxation.

From these data, it is clear that the clustered systems demonstrated a slightly higher electrical conductivity relative to the dispersed systems in all the alloy systems simulated. This observation is likely due to the different distributions of lattice distortions between the two configurations. Due to the differences between the atomic radii of the Al and solute atoms, lattice distortions occur at the solute atom sites. When the solute atoms are clustered, the total volume of distorted lattice at the Al-solute interface is reduced relative to the instance in which the solute atoms are dispersed. This reduced amount of interface lattice distortion results in a slightly more accessible electron conduction band, thus increasing the predicted electrical conductivity using the DFT method discussed above. From the data in Table 1, it appears that there is no clear trend between solute size and the overall electrical conductivity and relative conductivities between the clustered vs dispersed configurations. This indicates that the effect of solute atom size is small relative to the effects of dispersion and electronic structure characteristics. Since there was no significant change in free energy per atom between both configurations in all alloy systems

considered, the choice of using the clustered configurations for all remaining supercell calculations in this study was made for consistency purposes.

Table 1. Comparison of electrical conductivity and energy per atom in dispersed and clustered Al alloy systems. The percent increase in conductivity is also listed.

	σ_D fraction	E_D/atom (Disperse) (eV/atom)	Lattice constant (Disperse) (Å)	σ_C fraction	E_C/atom (Cluster) (eV/atom)	Lattice constant (Cluster) (Å)	%σ increase
Al_{108}	1.00	-3.76	12.0637	1.00	-3.76	12.0637	-
$Al_{106}Ni_2$	0.43	-3.825	12.0062	0.50	-3.825	12.0461	16.3
$Al_{106}Zr_2$	0.23	-3.900	12.1042	0.25	-3.897	12.0995	8.7
$Al_{106}Zn_2$	0.78	-3.709	12.0786	0.86	-3.709	12.0668	10.3
$Al_{106}ZnZr$	0.33	-3.804	12.0761	0.34	-3.804	12.1097	3.0
$Al_{106}ZnTi$	0.32	-3.786	12.0549	0.33	-3.785	12.0586	3.1
$Al_{106}ZnHf$	0.34	-3.825	12.0764	0.36	3.825	12.0771	5.9
$Al_{106}ZnV$	0.27	-3.772	12.0442	0.28	-3.771	12.0462	3.7
$Al_{106}ZnTa$	0.30	-3.828	12.0611	0.31	-3.821	12.0534	3.3
$Al_{106}ZnCr$	0.26	-3.789	12.0442	0.28	-3.789	12.0483	7.7
$Al_{106}ZnCo$	0.40	-3.765	12.012	0.43	-3.765	12.0262	7.5
$Al_{106}ZnNi$	0.49	-3.767	12.0331	0.55	-3.767	12.0353	12.2
$Al_{106}ZnCd$	0.74	1.913	12.0431	0.78	-1.913	12.0431	5.4
$Al_{106}NiZr$	0.23	-3.861	12.0325	0.27	-3.861	12.0664	17.4
$Al_{106}MgSi$	0.64	-3.879	12.0624	0.65	-3.879	12.0774	1.6

- Conductivity of each configuration is a fraction of that of pure aluminum
- σ_D and σ_C are normalized conductivities of disperse and cluster configurations, respectively
- E_D/atom and E_C/atom are the free energy per atom of disperse and cluster configurations, respectively

2.3. Pattern of electrical conductivity across transition elements

DFT simulations of FCC supercells of 108 atoms were constructed for a series of Al-TM binary systems to determine how the individual TMs affect the electrical conductivity in Al-TM binary systems. This information was important for validating the modeling with the experimental data[10]. Each system consisted of 107 atoms of aluminum and 1 atom (approx. 0.926 at. %) of TM. The same simulation parameters as described in the previous sub-section were used to predict the electrical conductivities of each alloy system. In Figure 3, the electrical conductivities for a series of Al-TM systems are plotted with respect to pure aluminum (thus, the

electrical conductivity of pure aluminum is normalized to 1, while those of Al-TM systems are expressed as fractions). Also shown in the figure are two sets of room temperature experimental values, based on the data in Figure 1. The series labeled as "expt-PPT" represents the true experimental result; it considers the effect of precipitation on conductivity once the maximum solubility limit of each transition metal in aluminum has been exceeded. The series "expt-SS" is the extrapolation of the data showing the decrease in conductivity per atomic percent of each transition metal in solid solution with aluminum according to Hatch[10]. The extrapolation of expt-SS ignores the solvus line (precipitation) effect on electrical conductivity, which is consistent with the DFT simulations. The trend of electrical conductivities computed using DFT agrees well with the experimental data (expt-SS) when precipitation is not considered and all solutes are assumed to remain in solid solution. The same cannot be said about expt-PPT. This is expected, because DFT simulations do not consider precipitation effects on electrical conductivity. However, similar to expt-SS and DFT curves, the expt-PPT data also shows an overall downward trend for the electrical conductivities of the Al-TM systems considered, though at a higher fraction of aluminum conductivity. Therefore, the overall electrical conductivity reduction observed for expt-PPT is lower than expt-SS. The lower conductivity reduction observed in expt-PPT is because once the composition of the solute atoms exceeds the solubility limit, the solute atoms that form precipitates do not degrade the conductivity as much as when in solution. Ni, Fe and Zr have a much higher electrical conductivity fraction for expt-PPT relative to expt-SS relative to Zn, Cu, V, Cr, Ti and Mn (Figure 3). This is because these elements have very small at.% solid solubility limit in aluminum (Figure 1). Therefore, the precipitation effect on their electrical conductivity values is more dominant since the majority of these solutes will precipitate out of solution.

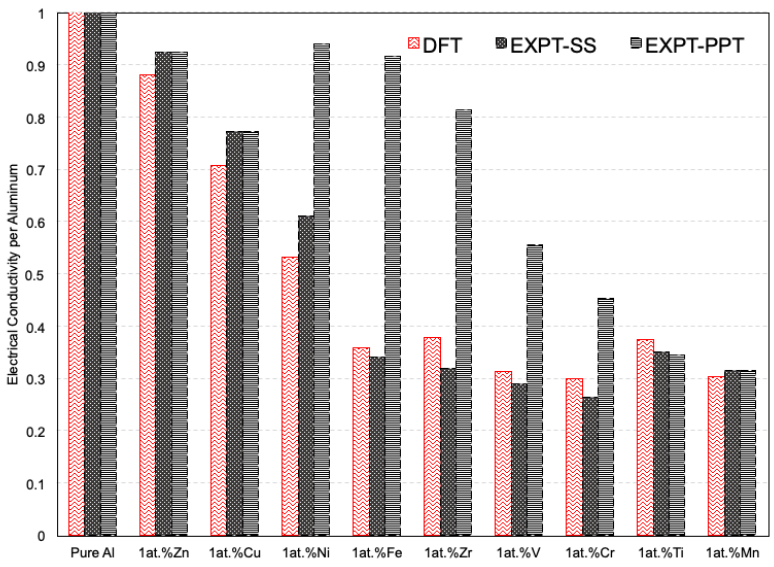

Figure 3. Comparison of electrical conductivity trends between experiment (precipitation and pure solid solution) and DFT. Except for pure Al, the alloy composition for each data point is Al-0.926 at. % TM.

After confirming modeling and experimental agreement in binary systems, fcc supercells (108 atoms) for a series of Al-Zn-TM ternary systems (TM = Sc, Y, Ti, Zr, Hf, V, Nb, Ta, Cr, Mo, W, Mn, Tc, Re, Fe, Ru, Os, Co, Rh, Ir, Ni, Cu, Ag, Au, Zn, Cd, Hg) were constructed and their electrical conductivities were predicted (Figure 4). Each system consisted of 106 atoms of Al and 1 atom each (approx. 0.926 at. %) of Zn and TM. The electrical conductivities are represented in bar chart format so that the overall trend of alloy conductivities within groups and across rows of the periodic table can be compared directly. According to the results shown in Figure 4, the predicted electrical conductivities show little change down each group from IIIB to VIIB, and a significant decrease down each of the groups VIII, IB, and IIB.

The DFT electrical conductivity trend of selected ternary alloys was compared to that of previous binary alloy data in Figure 3 to examine how including a third element (Zn) would alter the electrical conductivity trend of the binary alloys. According to Figure 5, the addition of Zn to binary Al-TM alloys to form ternary Al-Zn-TM showed similar electrical conductivity trends with slightly lesser values. The similarity between electrical conductivity values of Al-TM and Al-Zn-TM indicates that the addition of 1 at.% Zn to the binary Al-TM systems does not have significant negative impact on the electrical conductivities of the alloys. This agrees with the experimental observations shown in Figure 1.

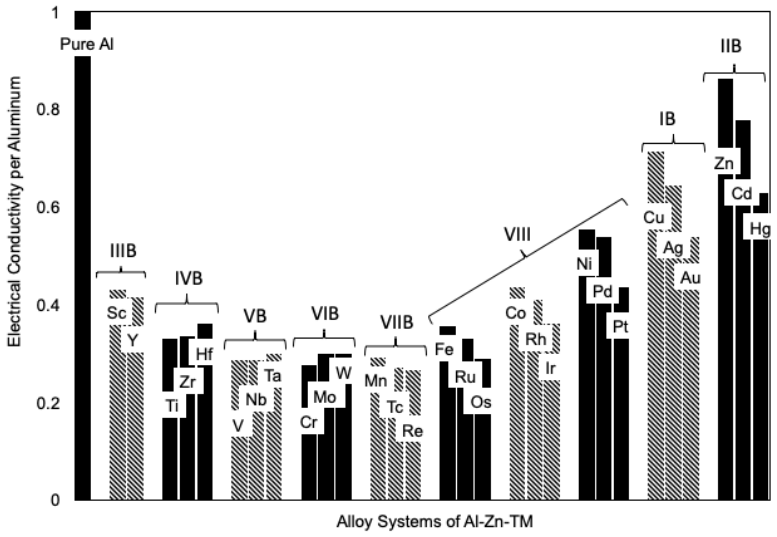

Figure 4. Electrical conductivity per aluminum of Al-Zn-TM formed across transition metals in the periodic table. Each block of solid and stripe pattern represents a group of transition metals.

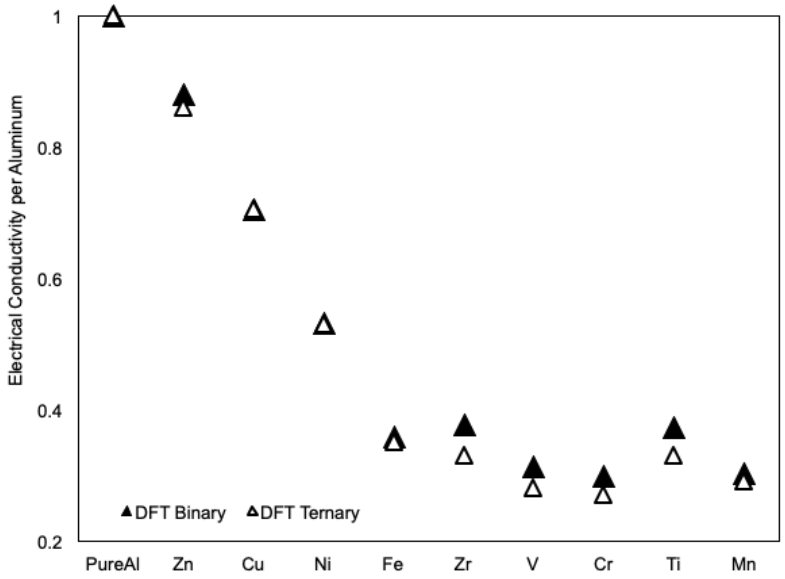

Figure 5. Comparison of the DFT electrical conductivity between binary Al-TM and ternary Al-Zn-TM. Except for pure Al, the alloy composition for each data point is Al-0.926 at.% TM for binary systems and Al-0.926 at.% Zn-0.926 at.% TM for ternary.

From Figure 4, the conductivities can be ranked in order from the highest to lowest as TM = Zn, Cd, Cu, Ag, Hg, Ni, Pd, Au, Co, Pt, Sc, Y, Rh, Ir, Hf, Fe, and Zr (there are still more elements with lower conductivity in Figure 4). In order to down-select TM candidates for further industrial development and commercial use, several factors were considered. First, considering alloy costs in the Al-Zn-TM alloy, relatively expensive elements such as Ag, Pd, Au, Pt, Sc, Rh and Ir were eliminated from consideration. Second, the avoidance of toxicity during fabrication is important, which eliminated Cd and Hg from consideration. Third, elements that do not aid the formation of $L1_2$ precipitate structure in Al-Zn-TM alloys, such as Cu and Co[28,42], were not considered. Finally, TM = Fe usually does solutionize for subsequent precipitation, and was thus eliminated from consideration. Therefore, the only remaining transition metal candidates considered further were TM = Ni, Zr, Y and Hf; and from these Ni and Zr were selected for this study because of their lower cost.

2.4. Equilibrium precipitate phase of alloy systems

The equilibrium phase structures of Al-Zn-Zr and Al-Zn-Ni aluminum alloy precipitates were investigated with DFT. The DFT approach was first used to simulate the most stable forms (unit cells) of pure Al, Zn, Ni, and Zr to determine their free energy per atom values. The unit cells from these models are shown in Figure 6.

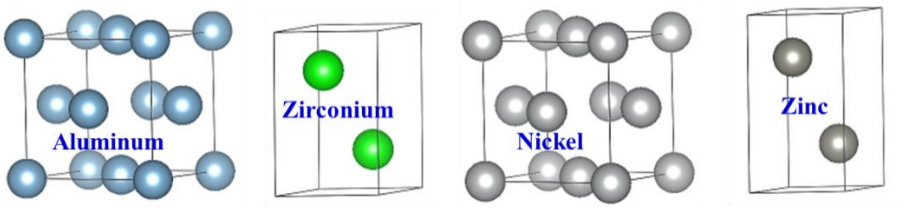

Figure 6. The most stable structures of pure Al (FCC), Zr (HCP), Ni (FCC), and Zn (HCP) from DFT simulation

Figure 7 shows the standard unit cells for the $L1_2$, $D0_{11}$, $D0_{22}$, and $D0_{23}$ structures. Because the $L1_2$ and $D0_{22}$ unit cells have fewer atoms than the $D0_{11}$ and $D0_{23}$ structures, they were scaled up to 16 atoms for direct comparison. Specifically, 1×1×4 and 1×1×2 arrays of $L1_2$ and $D0_{22}$ unit cells, respectively, were used to create supercells with 16 atoms each, to match the size of the $D0_{11}$ and $D0_{23}$ unit cells. For each simulation, an optimized plane-wave cutoff energy of 550 eV was used. Γ-centered Monkhorst-Pack grids were generated and optimized for each structure using the automatic mesh generation scheme implemented in VASP. Partial occupancies for each wavefunction were set using the method of Methfessel-Paxton as implemented in VASP. $D0_{23}$, $D0_{22}$ and $L1_2$ crystal structures were considered for both Al-Zn-Ni and Al-Zn-Zr alloy systems while orthorhombic $D0_{11}$ (which is the initial stable crystal structure of Al_3Ni prior to addition of Zn atoms) was considered only for the Al-Zn-Ni alloy.

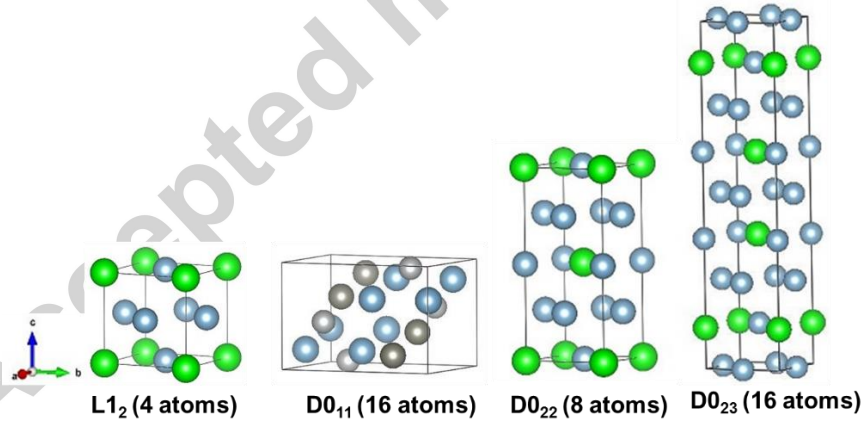

Figure 7. The unit cells of possible stable precipitates, consisting of aluminum (Blue atoms), Zn (grey atoms) and Zr (green atoms). $L1_2$ precipitate structure forms a coherent precipitate within the aluminum matrix, due to similarity in crystal structures and lattice parameters.

In order to determine the relative stability of the $L1_2$, $D0_{11}$, $D0_{22}$, and $D0_{23}$ phases for each Zn level in both systems, the enthalpy of formation at 0K was determined from the energy per atom (energy/atom) values obtained from DFT simulations and the equation:

$$\Delta H(Al-Zn-TM) = E(Al-Zn-TM) - aE(Al) - bE(Zn) - cE(TM) \qquad (5)$$

where ΔH is the enthalpy of formation; *E(Al-Zn-TM)*, *E(Al)*, *E(Zn)* and *E(TM)* are the energies per atom of the intermetallic compound, Al, Zn, and TM, respectively; and *a*, *b* and *c* are mole fractions of the corresponding elements. Each species was relaxed to its equilibrium geometry at zero pressure in the DFT simulations. The enthalpy of formation values for the Al-Zn-Ni and Al-Zn-Zr alloy systems are shown in Figure 8 and Figure 9 respectively, wherein the structure with the lowest enthalpy of formation for a given concentration of Zn is the most stable.

From Figure 8 it is apparent that the lowest energy structure of the Al_3Ni precipitate in the Al-Ni binary matrix is $D0_{11}$, which is incoherent with the matrix. However, there is a possibility of forming a $L1_2$ precipitate by replacing aluminum atoms in the precipitate structure with Zn atoms. Figure 8 shows that transformation of the $D0_{11}$ structure of Al_3Ni trialuminide to $D0_{23}$ occurs for very low Zn concentrations, and the subsequent transformation to $L1_2$ occurs at approximately 0.17 atomic fraction of Zn (assuming a linear interpolation between data points). The $L1_2$ crystal structure continues to be most probable for Zn concentrations up to 0.5, at which point the $D0_{22}$ phase has a nearly equal enthalpy of formation. Similarly, from Figure 9, the initial Al_3Zr precipitate phase has a theoretical equilibrium $D0_{23}$ crystal structure even though experimentally it has been observed that during heat treatment, the Al_3Zr precipitates formed assume a metastable $L1_2$ structure at temperature $< 475\ ℃$[12]. At a Zn concentration of about ≥ 0.04, the most stable crystal structure of the intermetallic becomes $L1_2$, which remains the most stable for higher Zn concentrations as shown in the graph[29]. Thus, it is evident from the simulations that the $Al_{3-x}Zn_xNi$ and $Al_{3-x}Zn_xZr$ precipitates formed in Al-Zn-Ni and Al-Zn-Zr alloy systems, respectively, have a coherent $L1_2$ structure, which is necessary for more effective material strengthening.

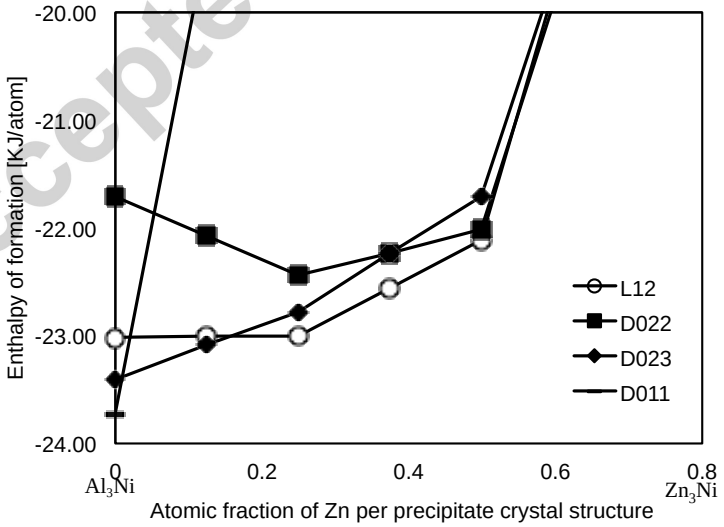

Figure 8. Enthalpy of formation of the Al-Zn-Ni alloy system. The $L1_2$ crystal structure becomes most stable at 0.17 atomic fraction of Zn.

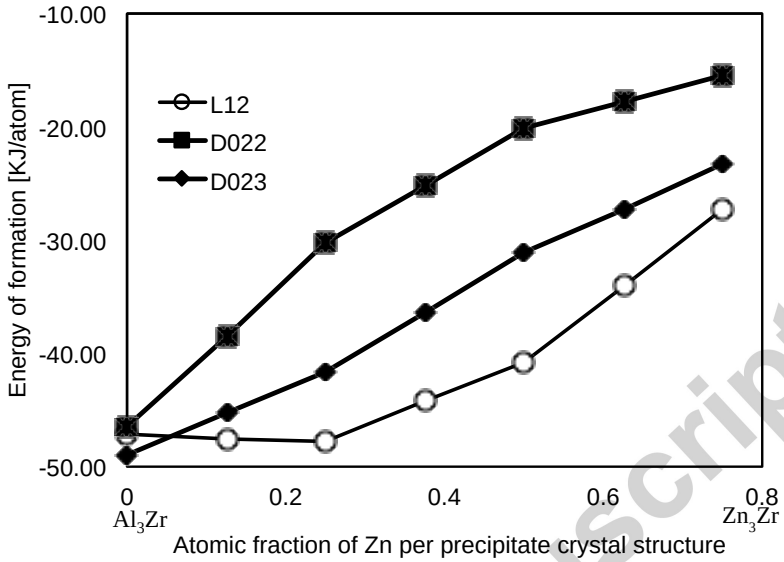

Figure 9. Enthalpy of formation of the Al-Zn-Zr alloy system. The $L1_2$ crystal structure becomes most stable at a 0.04 atomic fraction of Zn.

3. Experimental methods

Based on the electrical conductivity and thermodynamic phase stability results from the DFT computational simulations discussed above, Al-Zn-Ni and Al-Zn-Zr alloys were identified as having moderate to high conductivities and the ability to form $L1_2$ precipitate structures necessary for improved strength. Additionally, compared to other Al-Zn-TM alloys, Ni and Zr were expected to be inexpensive, not involve any toxic metals, have low diffusivity, and be highly castable. The next step in the ICME process was to fabricate samples of the Al-Zn-Ni and Al-Zn-Zr systems for characterization and mechanical and electrical testing. In this section, the fabrication and testing procedures are described, and the test results for Al-Zn-Ni and Al-Zn-Zr are compared.

3.1. Fabrication and testing of Al-Zn-Ni and Al-Zn-Zr

Four different 600-gram ingots of Al-Zn-Ni and two 600-gram ingots of Al-Zn-Zr alloys were fabricated from 99.99 wt.% purity aluminum, Al–20 wt.% Ni and Al–5 wt.% Zr master alloys, and 99.99 wt.% purity Zn ingots in a vacuum induction melter (VIM). Measured quantities of each component were arranged inside a graphite crucible within the VIM chamber. A vacuum pressure of 7.8×10^{-5} Torr was obtained inside the chamber through the use of a diffusion pump to minimize reactive gases before partially backfilling to 558 Torr with 99.999 wt.% Ar gas. The temperature (measured by an optical pyrometer above the crucible) was gradually ramped to 710 ℃, thereby melting the components inside the crucible. The target and nominal compositions of

the alloys are listed in Table 2. Small size buttons were cut out of the 19 mm diameter rods of each ingot and their compositions measured using Inductively Coupled Plasma Optical Emission Spectroscopy (ICP-OES). The small buttons from the ingots were polished for optical metallography using 180, 320, 600 and 1500 silicon carbide paper grit followed by 6 μm diamond, 1 μm diamond, and a 0.04 μm silica solution polishing pads.

Solid solution heat treatments were performed on the Al-Zn-Ni samples for 4 hours at 620 ℃, within the single phase region so as to homogenize the Ni solute, before quenching in cold water. Without prior homogenization of Al-Zn-Ni specimens, a microhardness increase was not observed during aging. The Al-Zn-Zr alloys were not homogenized because prior homogenization of Al-Zr alloy first nucleates primary Al_3Zr precipitates. This reduces the amount of Zr solute left in solid solution for subsequent aging, thereby leading to a corresponding lower peak microhardness from precipitation hardening[30]. A series of multi-step isochronal aging experiments were carried out on the alloy buttons from 150 to 400 $°C$ at 50 $°C$ temperature steps and 150 to 600 $°C$ at 50 $°C$ temperature steps for Al-Zn-Ni and Al-Zn-Zr, respectively. The duration for each temperature step was 3 h in the furnace before quenching in water.

Vickers microhardness measurements were performed on the mechanically polished surface at every temperature step, with a load of 50 g and dwell time of 15 s. A calibrated Sigmascope SMP10 probe was used for electrical conductivity measurements of each button specimen.

3.2. TEM analysis

For TEM analysis, thin foils (200 μm thickness) were cut out from samples of 0.5Zn0.05Ni, 1.0Zn0.05Ni, 1.8Zn0.05Ni and 1.7Zn0.07Zr. These foils were then mechanically polished down to < 100 μm. An FTS System Multicool chiller connected to the Jet Electropolisher was used to maintain the temperature of 150 ml methanol and 60 ml nitric acid mixture (electrolyte) at -35 $°C$ before electropolishing was performed on the samples at 10 V (~ 70 mA). The TEM imaging used an FEI Titan Themis Scanning-Transmission Electron Microscopy (S-TEM) operating at 200 kV. Energy Dispersive X-ray Spectroscopy (EDX) analysis was performed on the samples with the use of Bruker software.

Table 2. Sample labels and composition in at.% (ICP OES)

Sample Label	Al	Target Zn	Actual Zn	Target Ni	Actual Ni	Target Zr	Actual Zr
0.5Zn0.05Ni	Bal	0.5	0.51	0.05	0.05	-	-
1.0Zn0.05Ni	Bal	1.0	1.02	0.05	0.04	-	-
1.8Zn0.05Ni	Bal	1.5	1.80	0.05	0.07	-	-
0.5Zn0.10Ni	Bal	0.5	0.50	0.1	0.08	-	-
1.0Zn0.07Zr	Bal	1.0	1.00	-	-	0.075	0.06
1.7Zn0.07Zr	Bal	1.5	1.70	-	-	0.075	0.06

4. Experimental results

The results obtained from the experiments described in Section 3 for the two material systems identified in Section 2 are presented below. The Al-Zn-Ni system is reported first followed by the Al-Zn-Zr system.

4.1. Multi-step isochronal aging of Al-Zn-Ni

Figure 10 shows the conductivity and microhardness of multi-step isochronally aged Al-Zn-Ni with 50 $°C$ temperature steps. The peak microhardness values of all the Al-Zn-Ni alloys were observed at an aging temperature of 250 $°C$. Alloys 0.5Zn0.05Ni and 1.8Zn0.05Ni have similar Ni compositions but different Zn levels (see Table 2 for exact composition). An increase of Zn composition from 0.5 to 1.8 at.% improved the alloy microhardness at all aging temperatures. The peak microhardness achieved for 0.5Zn0.05Ni, 1.0Zn0.05Ni, 1.8Zn0.05Ni, and 0.5Zn0.1Ni were 337, 341, 376 and 328 MPa, respectively. The average increase in microhardness due to precipitation of Al-Zn-Ni system is approx. 28%. Comparison of 0.5Zn0.05Ni and 0.5Zn0.1Ni, which have the same Zn level but different Ni content (Table 2), indicates that increasing Ni from 0.05 to 0.08 at.% yields a slightly higher microhardness in the as-solutionized state but reduces the peak microhardness at 250 $°C$. Beyond 250 $°C$, the microhardness of all Al-Zn-Ni samples continued to drop until they reached their as-cast/pre-aging microhardness due to over-aging and precipitate dissolution. During over-aging, precipitate mean size increases as a result of growth and subsequent coarsening also known as Ostwald Ripening. This increases the edge-to-edge precipitate spacing, thereby allowing dislocations to move more freely between precipitates.

An increase in Zn level reduced the conductivity from 35.1 (0.5Zn0.05Ni) to 32.3 MS/m (1.8Zn0.05Ni) mostly due to the presence of more Zn solute in solid solution. The effect of increasing Ni composition from 0.05 at.% (0.5Zn0.05Ni) to 0.08 at.% (0.5Zn0.1Ni) on conductivity is negligible (they are both approximately 35.1 MS/m) because Ni has a very minimal negative effect on conductivity of aluminum alloys when precipitated out of solution[10]. For all aging temperatures, the conductivities of Al-Zn-Ni alloys remained almost constant.

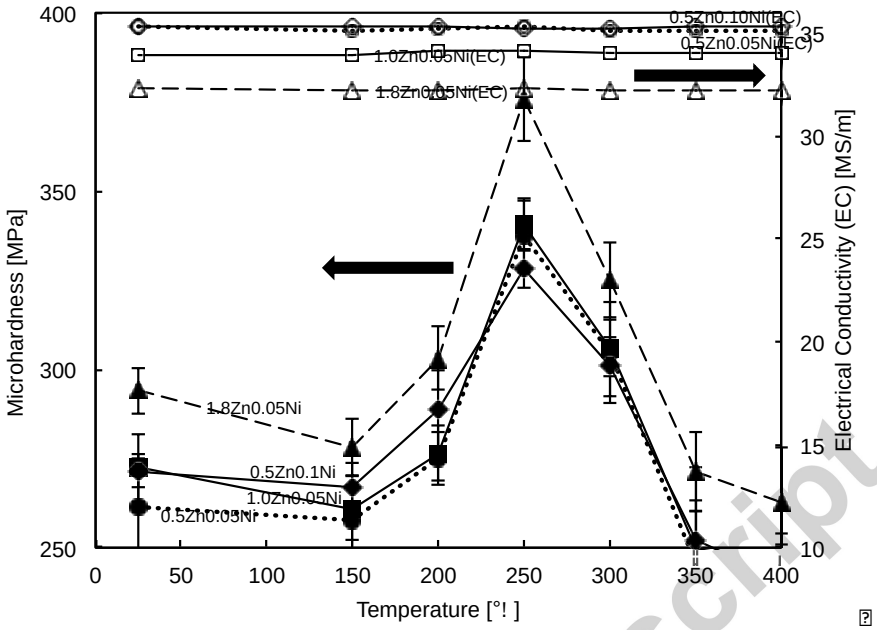

Figure 10. Conductivity and microhardness of Al-Zn-Ni as a function of aging temperature for a 3 h multi-step isochronal annealing with temperature increments of 50 °C.

4.2. Multi-step isochronal aging of Al-Zn-Zr

Results from isochronal aging of homogenized Al-Zn-Zr samples are shown in Figure 11. The purpose was to observe the peak microhardness, the aging temperature at which peak microhardness occurs, and the conductivity of the Al-Zn-Zr alloys; and to compare these values to those of the Al-Zn-Ni alloys. In this alloy system, peak microhardness occurs at 450 °C, which is 200 °C higher than that of Al-Zn-Ni. The increase in Zn composition increased the peak microhardness while reducing the electrical conductivity. The 1.0Zn0.07Zr and 1.7Zn0.07Zr systems have peak microhardness values of 441 and 458 MPa, while their conductivities are 31.8 MS/m and 30.1 MS/m, respectively. The similar microhardness difference between both alloys at as-cast (14 MPa) and peak-aged conditions (17 MPa) indicates mostly solid solution strengthening from the excess Zn between them. Hence, increasing Zn composition does not increase precipitate volume fraction. The microhardness values of Al-Zn-Zr are much higher than the equivalent composition of Al-Zn-Ni alloys. However, they have lower electrical conductivities than Al-Zn-Ni. For instance, 1.7Zn0.07Zr (Al–1.7 at.% Zn–0.06 at.% Zr) has a peak microhardness of 458 MPa and conductivity of 30.1 MS/m at approximately 450 °C (Figure 11), compared to 376 MPa and 32.2 MS/m in 1.8Zn0.05Ni (Al–1.8 at.% Zn–0.07 at.% Ni) at 250 °C (Figure 10). Even though 1.7Zn0.07Zr has similar at.% of Zn and Zr to the compositions of Zn and Ni in 1.8Zn0.05Ni. The peak conductivity occurred at ~475 °C due to the precipitation of solutes out of solution. The subsequent reduction in conductivity after the peak condition is due to the precipitate coarsening and dissolution as the aging temperature continued to increase. Similarly, over-aging leads to the strength reduction of Al-Zn-Zr alloys to their as-cast microhardness due to coarsening.

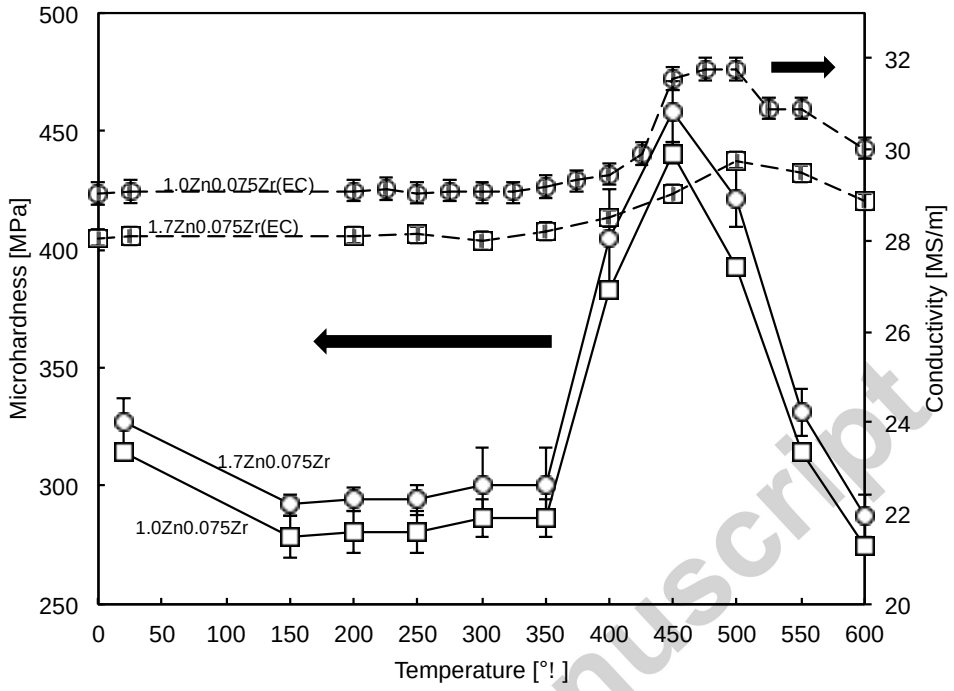

Figure 11. Conductivity and microhardness of Al-Zn-Zr as a function of aging temperature (3 h multi-step isochronal).

4.3. TEM study of Al-Zn-Ni

The small precipitates formed in 0.5Zn0.05Ni, 1.0Zn0.05Ni, and 1.8Zn0.05Ni specimens after aging at 250 $°C$ have a mean size of $\leq 10\,nm$. The orientation of needle-like uniformly distributed particles, present in 0.5Zn0.05Ni and 1.0Zn0.05Ni, is along the longitudinal section (Figure 12a,b). However, coherent spheroidal particles, (Figure 12c), were present in the 1.8Zn0.05Ni specimen, which has a higher amount of Zn solute. This precipitate/matrix coherency in 1.8Zn0.05Ni is indicated by the Ashby-Brown strain contrast. The diffraction patterns acquired from the Al-Zn-Ni specimens at 250 $°C$ showed no ordered superlattice spots that could be attributed to the precipitate phase. Only fcc planes were observed. The reason for this could be a combination of the small size or volume fraction of the precipitates. To increase the likelihood of detecting the precipitate phase structure from the diffraction pattern, the beam was converged on the large precipitate formed in the overaged specimens after aging at 400 $°C$. Specifically, needle-like precipitates were found in the 0.5Zn0.05Ni and 1.0Zn0.05Ni specimens (Figure 12d,e). The diffraction pattern along the z[100] indicates that these precipitates have a $D0_{11}$ structure, which is the typical crystal structure of Al_3Ni. Precipitates formed in 1.8Zn0.05Ni maintained spheroidal morphology at an overaged temperature (Figure 12f) with a slightly visible line of no contrast. The $(00\bar{1})$ and $(01\bar{1})$ superlattice spots present in the SAED acquired along z[100] show that these spheroidal particles most likely have $L1_2$ precipitate structure.

EDX chemical composition analysis indicates that the 0.5Zn0.05Ni and 1.0Zn0.05Ni specimens have no Zn species present in their precipitate phases, while the spheroidal particles in 1.8Zn0.05Ni are rich in Zn. When the electron beam was converged on just the matrix region versus a single precipitate, the EDX data showed that all the Ni species were contained in the precipitate phase; no Ni was present in the matrix. Quantitatively, 0.5Zn0.05Ni and 1.0Zn0.05Ni alloys are likely to have a precipitate stoichiometry of Al_3Ni. However, since there was a measurable amount of Zn present in the precipitates formed in 1.8Zn0.05Ni, they are presumed to have the form $Al_{3-x}Zn_xNi$[15]. The compositions of the precipitates and matrix of the Al-Zn-Ni alloys are summarized in Table 3.

At 400 $°C$, the average length of the needlelike particles in 0.5Zn0.05Ni and 1.0Zn0.05Ni is between 60 and 250 nm, while the average interparticle spacing for both alloys varies from 80 to 400 nm (Figure 12d,e). From observation, increasing the composition of Zn from 0.5 to 1.0 at.% translated into bigger mean precipitate size in 1.0Zn0.05Ni relative to 0.5Zn0.05Ni. The overaged spheroidal precipitates formed in 1.8Zn0.05Ni have a mean particle diameter of 25 nm as shown in Figure 12f.

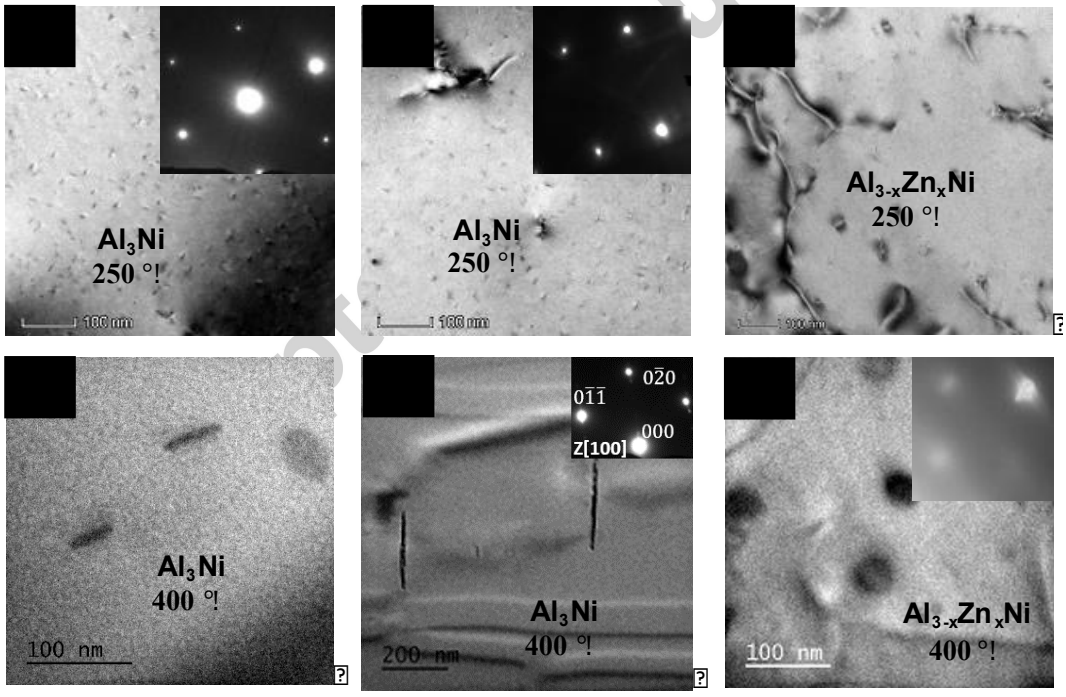

Figure 12. TEM images showing the microstructures of precipitates formed in Al-Zn-Ni alloy specimens at 250 and 400 $°C$, (a & d) 0.51 at. % Zn, (b & e) 1.02 at. % Zn and (c & f) 1.8 at.% Zn. TEM images of the overaged specimens were observed along the [100] zone axis. The observed phase structures of the precipitates are $D0_{11}$ for 0.5Zn0.05Ni and 1.0Zn0.05Ni, and coherent $L1_2$ for 1.8Zn0.05Ni.

4.4. TEM study of Al-Zn-Zr

The microstructure and diffraction patterns (matrix and precipitate) of the 1.7Zn0.07Zr Al alloy isochronally peak-aged at 450 $°C$ were observed under TEM. Figure 13a,b shows a high and low number density of precipitates with spheroidal morphology dispersed in the dendritic center and interdendritic channel, respectively. There was a lateral gradient of precipitate sizes from the dendritic center toward the interdendritic channel of the specimen. A similar mean size gradient has been reported for Al-Zr alloys[12]. The particles present in the dendritic center have a mean diameter of $< 5\ nm$, while those in the interdendritic channels are bigger in size, with a mean diameter of ~17 nm and inter-particle spacing of 80 – 100 nm. The Ashby-Brown strain contrast in Figure 13c indicates precipitate/matrix coherency. From the SAED, it was observed that in addition to the expected fcc planes such as $(\bar{2}20)$ and $(\bar{3}13)$, there are other smaller superlattice spots that are attributed to the presence of $L1_2 - \{110\}$ planes. These indicate that the precipitates formed in Al-Zn-Zr have a $L1_2$ crystal structure. The TEM images of this specimen were collected along the [332] zone axis. Other diffraction patterns along low index zone axes [111] and [110] (not included in this paper) were collected, further showing that the $Al_{3-x}Zn_xZr$ precipitate phase is $L1_2$.

EDX data obtained when the beam was converged on the matrix or spheroidal precipitate regions of the 1.7Zn0.07Zr system shows that there is a high concentration of Zr in the precipitates phase relative to the matrix. The compositions of the precipitates and matrix are summarized in Table 3. As with the Ni alloy, the matrix had no Zr atoms present.

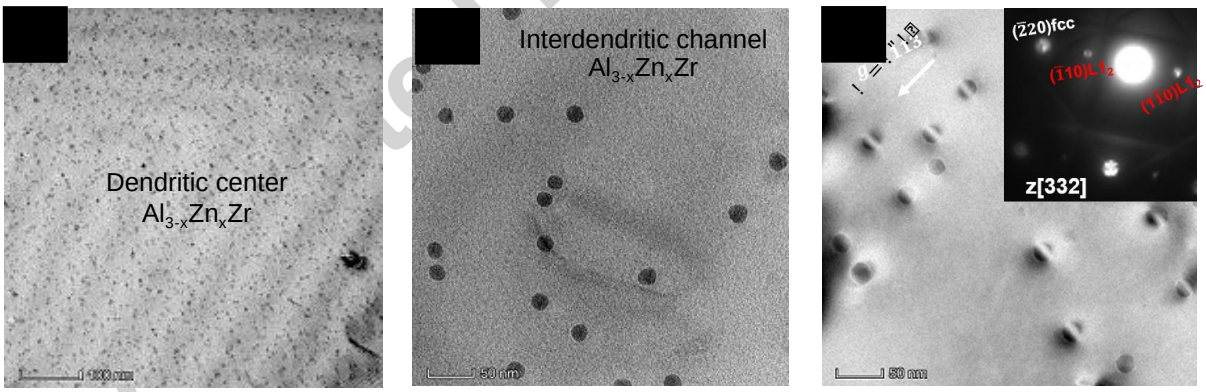

Figure 13. TEM images showing the microstructures and diffraction patterns of 1.7Zn0.07Zr alloys: (a) Small spheroidal $Al_{3-x}Zn_xZr$ precipitates of $< 5\ nm$ diameter formed at the center of the dendrites. (b) At the interdendritic channels, bigger $L1_2$-$Al_{3-x}Zn_xZr$ precipitates of 17 nm diameter were present. (c) Shows the corresponding Ashby-Brown strain contrast of the coherent $Al_{3-x}Zn_xZr$ precipitates within the same interdendritic channel, with the diffraction pattern obtained along [332] zone axis showing the {110} plane. This indicates that the precipitate phase has an $L1_2$ ordered lattice structure.

Table 3. Summary of EDX data of Al-Zn-Ni and Al-Zn-Zr (at. %) at peak aged conditions

Specimens		Al	Zn	Ni	Zr
0.5Zn0.05Ni	Precipitate	75.1	-	24.9	-
	Matrix	99.5	0.5	-	-
1.0Z n0.05Ni	Precipitate	75.0	-	25.0	-
	Matrix	99.0	1.0	-	-
1.8Zn0.05Ni	Precipitate	69.3	5.9	24.8	-
	Matrix	98.3	1.7	-	-
1.7Z n0.07Zr	Precipitate	70.1	5.1	-	24.8
	Matrix	99.1	1.6	-	-

5. Discussion

5.1. Comparing microhardness of Al-Zn-Ni and Al-Zn-Zr

From Figures 10 and 11, the first sign of nucleation occurs after 150 and 350 ℃ for Al-Zn-Ni and Al-Zn-Zr, respectively. This indicates that the presence of Ni in the Al-Zn-TM alloy decreased the incubation time for precipitate nucleation compared to Zr. As precipitates formed in Al-Zn-Ni nucleate at > 150 ℃, continued increase of aging temperature led to precipitate growth. At 250 ℃, a critical precipitate diameter was reached, and peak microhardness was observed. Between 150 and 250 ℃, there was no sign of nucleation in the Al-Zn-Zr alloy. The peak microhardness for this alloy was attained after aging up to 450 ℃. The lower peak microhardness temperature observed in Al-Zn-Ni relative to Al-Zn-Zr suggests that the precipitates formed in Al-Zn-Zr are more stable to higher temperatures compared to Al-Zn-Ni. The difference between their peak microhardness temperatures can be attributed to the higher diffusivity of Ni in Al relative to that of Zr in Al at every aging temperature, as shown in Table 4. Precipitation growth is controlled by the diffusion of solute atoms in the solvent at specific aging temperatures. At any particular aging temperature, the diffusivity of the solute atoms in the solvent has a direct influence on the distance covered by the solute from its supersaturated position to the nearby nucleation site. The higher the diffusivity, the faster the precipitates grow. The diffusivity and diffusion distance of various elements (used in this study) at 250 and 450 ℃ were estimated by an Arhenius relationship, $D = D_o \exp(-Q/R_g T)$, using their respective activation enthalpy Q and pre-exponential D_o values[11,30,31,32]. For precipitate growth to occur at specific aging temperatures, the solutes would require sufficient heat energy to migrate from their supersaturation position to a nearby nucleation site. In general, the distance traveled by the solutes should be reasonably close to the average interparticle spacing at that aging temperature.

Table 4. Diffusion and distance data for selected transition metal (3d and 4d) solutes in aluminum at 250 and 450 ºC[11].

	Pre-exponential D_o (m^2s^{-1})	Activation Enthalpy, Q (KJ/mol)	D at 250 ºC (m^2s^{-1})	Diffusion distance (nm) at 250 ºC after 3hrs	References
			Self-Diffusion		
Al	1.37×10^{-5}	124	3.25×10^{-15}	349	[33]
			3d and 4d-Transition metals		
Ni	4.4×10^{-4}	148	2.05×10^{-15}	125	[34]
Zn	2.59×10^{-5}	121	2.13×10^{-17}	480	[35]
Zr	7.28×10^{-2}	242	4.92×10^{-26}	0.0325	[36]
	Pre-exponential D_o (m^2s^{-1})	Activation Enthalpy, Q (KJ/mol)	D at 450 ºC (m^2s^{-1})	Diffusion distance (nm) at 450 ºC after 3hrs	References
Zr	7.28×10^{-2}	242	2.38×10^{-19}	72 nm	[37]

After aging at $250\,℃$ for 3 h, only Al, Zn, and Ni solute species would cover distances $> 120\,nm$, while Zr would cover only 0.0325 nm. Considering that the average interparticle spacing for 1.8Zn0.05Ni is 80 – 200 nm, the Zn and Ni solutes have sufficient driving force to reach a nearby nucleation site, which leads to precipitate growth. The distance covered by Zr at this temperature makes it unlikely that any $Al_{3-x}Zn_xZr$ precipitate growth would happen. It also explains why Zr alloys require a higher temperature for the formation and growth of its strengthening phase. Zr atoms move 72 nm after aging at 450 ºC for 3 h (Table 4), which is far enough to reach the nearby precipitate phase, since the interparticle spacing for 1.7Zn0.07Zr is between 10-15 nm (dendritic center) and 20-80 nm (interdendritic channel). Beyond the peak microhardness conditions for both alloys, the precipitates continue to grow and become bigger than the critical size, as more solutes migrate into the precipitate phase. As a result, the precipitates become harder, thereby, requiring more force for dislocations to shear instead of bowing through. The early stage of overaging, between 250 – 300 ºC (1.8Zn0.05Ni) and 450 – 500 ºC (1.7Zn0.07Zr), is controlled by dislocation bowing (Orowan strengthening). This is followed by precipitate coarsening and dissolution of solutes from the precipitate phase into the matrix at the latter stage of overaging. Here the bigger precipitates grow at the expense of smaller ones. The influence of precipitation on the microhardness of the alloys becomes insignificant at this stage as the hardness of the alloy mostly depends on solid solution strengthening from the dissolved solutes[38]. Hence, the microhardness values of the specimens return to the as-cast microhardness state at 400 and 600 ºC for 1.8Zn0.05Ni and 1.7Zn0.07Zr, respectively.

5.2. Electrical conductivity

The heat treatment results presented in Figure 10 and 11 also show a consistent reduction in conductivity as Zn composition increases. Since most of the Zn remains in solid solution, the

trend of reduced conductivity is due to the increase in local electron scattering sites as a result of the presence of Zn solute atoms within the Al matrix. The increase in conductivity of the Al-Zn-Zr alloys (1.7Zn0.07Zr and 1.0Zn0.07Zr) observed at 475 ºC in Figure 11 is due to the precipitation of the solute atoms out of solution (especially Zr; Figure 1). When in solid solution, alloying elements contribute to the lattice distortion of the matrix and generation of local electron scattering sites, which reduce the mobility of free electrons in the system[39]. The creation of lattice distortion by the solutes in solid solution is driven by the dissimilar atomic radii of the solute and solvent atoms[39]. However, during precipitation, the solute atoms form a secondary phase with a different composition and structure from the matrix, thus reducing their contribution to the lattice distortion and local electron scattering. Hence, the mobility of free electrons within the system is less hindered, leading to the increased conductivity observed. A similar increase in conductivity was not observed in Al-Zn-Ni alloys as shown in Figure 10. The lower electrical conductivity observed in Al-Zn-Zr (1.0Zn0.07Zr and 1.7Zn0.07Zr) relative to Al-Zn-Ni (1.0Zn0.05Ni and 1.8Zn0.05Ni) is due in large part to the role of Zr in electrical conductivity degradation relative to Ni (Figure 1). Unlike Zr, Zn and Ni do not have a severe impact on the electrical conductivity of aluminum alloys. The more damaging impact of Zr on the electrical conductivity of aluminum, relative to Zn and Ni, was already predicted by the DFT simulation results for Al-TM and Al-Zn-TM shown in Figures 3 and 4.

5.3. Microstructure of Al-Zn-Ni and Al-Zn-Zr

For the precipitates of the aged Al-Zn-Ni alloys to transform into the $L1_2$ structure of spheroidal morphology, a critical quantity of Zn must be present in the precipitate phase according to DFT simulation results (Figures 8 and 9). The needle-like morphology of the particles observed in 0.5Zn0.05Ni and 1.0Zn0.05Ni (Figure 12) represents the formation of an Al_3Ni intermetallic. This is supported by EDX chemical composition analysis, which shows that there is no Zn present in the precipitate phase of 0.5Zn0.05Ni and 1.0Zn0.05Ni. The diffraction patterns shown in Figure 12d,e confirm their precipitate structures as orthorhombic $D0_{11}$. Al_3Ni has a $D0_{11}$ Fe_3C-type cementite structure that has a needlelike particle shape, indicating an orthorhombic crystal structure[40,41]. From the ternary phase diagram of Al-Zn-Ni, the maximum solubility limits of Zn in aluminum at room temperature and 250 ºC (peak aging) are 0.69 and 10 at.%, respectively[42]. Considering that 0.5Zn0.05Ni and 1.0Zn0.05Ni alloys have 0.51 and 1.02 at.% Zn respectively, these solubility limits are significantly higher. Therefore, it is possible that most of the Zn remained in solution after quenching the alloys to room temperature and during subsequent aging. This could explain why the precipitate morphologies were non-$L1_2$ ($D0_{11}$) with no Zn present in the precipitate phase. It is also possible that the excess Zn that precipitated out of solution while aging 1.0Zn0.05Ni diffused into the precipitate phase but was insufficient to transform the precipitate structure from $D0_{11}$ to coherent $L1_2$ (Figure 8). The spheroidal particles shown in Figure 12c,f for 1.8Zn0.05Ni indicate that there is a sufficient amount of Zn atoms entering the precipitate phase from the saturated solid solution. The presence of these Zn atoms allows for the transformation of the precipitate morphology from Al_3Ni, which has the needlelike orthorhombic $D0_{11}$ structure,[11,40,41,43] to $Al_{3-x}Zn_xNi$ with the spheroidal $L1_2$ form. The structure of $Al_{3-x}Zn_xNi$ present in 1.8Zn0.05Ni is confirmed as $L1_2$ by the diffraction pattern shown in

Figure 12f inset[44]. During nucleation, the lower Gibbs free energy associated with Zn in the particles (instead of the matrix) serves as the driving force for Zn to migrate from the matrix into the precipitate phase. There is also a solute concentration gradient between the matrix and the precipitates phases, which influences the solute diffusion direction.

As shown in Figure 13, there is a precipitate size gradient observed in 1.7Zn0.07Zr. This size gradient is a result of the microsegregation of Zr solute in the alloy while solidifying during casting. The Zr solutes segregate into dendritic centers and interdendritic channels[12]. The high concentration of Zr in the dendritic center increases the chemical driving force for precipitate nucleation. Therefore, the critical mean radius for nucleation to occur is reduced and smaller precipitates are formed. For the interdendritic channels (Figure 13b) the mean precipitate size is bigger due to low Zr solute concentration and a lower chemical driving force for nucleation. Similar to the morphology of Al_3Zr precipitates reported in several studies[12,13], $Al_{3-x}Zn_xZr$ precipitates have a spheroidal form with lines of no contrast perpendicular to the $g = 313$ vector (Figure 13c). The SAED information obtained along the [332] zone axis shows additional weak {110} superlattice spots, which confirms that the $Al_{3-x}Zn_xZr$ precipitate has an ordered lattice structure corresponding to the $L1_2$ phase. This demonstrates that including Zn into the precipitate phase structure does not alter the metastable $L1_2$ phase structure previously reported for Al_3Zr. Therefore, while attempting to improve the alloy strength with Zn, the $L1_2$ precipitate phase structure and high electrical conductivity were maintained. According to EDX chemical composition analyses (Table 3) the absence of Zr in the matrix indicates that Zr solute atoms precipitated out of solid solution to form coherent $Al_{3-x}Zn_xZr$ precipitates. It also shows that a small fraction of Zn was used up in the precipitate phase.

5.4. Estimation of yield strength at peak conditions

According to Figures 10 and 11, the observed maximum yield strengths for 1.8Zn0.05Ni and 1.7Zn0.07Zr are ~125 (250 ℃) and ~156 MPa (450 ℃), respectively, using a conversion factor of $\frac{1}{3}$ between Vickers microhardness and yield strength[45]. These observed strengths are due to solid solution and precipitation strengthening mechanisms. Grain size reduction and strain hardening of the specimens were not considered since aging is not expected to have any significant effect on grain size and the specimens were not deformed. The yield strengths of the specimens have contributions from modulus mismatch, order, Orowan, and coherency strengthening mechanisms due to the spheroidal coherent precipitates formed during aging. The relative contributions of these mechanisms can be quantified as follows.

Modulus mismatch strengthening, $\Delta\sigma_{ms}$, results from the difference between the shear moduli of the precipitate and matrix phases. It can be estimated by using[46,63]:

$$\Delta\sigma_{ms} = 0.0055M(\Delta G)^{3/2}\left(\frac{2\phi}{G_{Al}}\right)^{1/2}\left(\frac{\langle R\rangle}{b}\right)^{3m/2-1} \qquad (6)$$

where the Taylor factor[47] $M = 3.06$ and ΔG is the difference in the shear modulus between the precipitate and matrix, which are approximated as 30.6 and 40 GPa for $Al_{3-x}Zn_xNi$ and $Al_{3-x}Zn_xZr$, respectively. The shear moduli of $L1_2$-type $Al_{3-x}Zn_xNi$, $Al_{3-x}Zn_xZr$, and the matrix are

taken as $G_{\mathrm{Al3-xZnxNi}} = 56$ GPa (same as the value for Al_3Ni[4,48]), $G_{\mathrm{Al3-xZnxZr}} = 67.4$ GPa (same as the value for Al_3Zr [49,50,51]), and $G_{Al} = 25.4\,GPa$, respectively. The volume fraction was approximated as $\phi \cong 0.003$ (estimated from the tie line of the Al_3Zr phase diagram) for $Al_{(3-x)}Zn_xZr$. Since the added Zn is assumed to replace the Al site, it is expected that Al_3Zr and $Al_{(3-x)}Zn_xZr$ have similar volume fractions[52]. This assumption is also confirmed by the heat treatment curves. Using the same approach, $\phi \cong 0.002$ for $Al_{(3-x)}Zn_xNi$. $\langle R \rangle$ is the average particle radius of the specimens. Due to their large number density and small interparticle spacing, most of the precipitation strengthening of 1.7Zn0.07Zr comes from the small size particles segregated in the dendritic centers. Hence, the values of $\langle R \rangle$ used for the yield strength estimates were $2.5\,nm$ (dendrite core) and $4.0\,nm$ for the precipitates present in 1.7Zn0.07Zr and 1.8Zn0.05Ni, respectively (Table 5). The Burgers vector magnitude of the matrix was[53,54] $b = 0.286\,nm$ and m = 0.85 is a constant.

At peak strength, order strengthening $\Delta\sigma_{os}$ (which is due to the formation of antiphase boundaries (APBs) as matrix dislocations shear ordered particles) is given by[46,65,63]:

$$\Delta\sigma_{os} = 0.81M\frac{\gamma_{APB}}{2b}\left(\frac{3\pi\phi}{8}\right)^{1/2} \qquad (7)$$

where γ_{APB} ~0.48 and $0.445\,Jm^{-2}$ are taken as the average APB energies for $Al_{3-x}Zn_xNi$ and $Al_{3-x}Zn_xZr$ alloys, respectively, based on several reported values for Al_3Ni and Al_3Zr for the (111) plane[55,56,57]. APB energies are difficult to determine, and different methods tend to give varying values for the same intermetallic compound. Therefore, APB energies have only been reported for a limited number of compounds[58,59,60]. Recently, Rudy and Sauthoff reported a APB energy of $\sim 0.4\,Jm^{-2}$ for NiAl[61]. A study has already reported the APB energy for Ni_3Al $\sim 0.195\,Jm^{-2}$[62].

During over-aging, Orowan strengthening $\Delta\sigma_{or}$ is given by[46,65,63]:

$$\Delta\sigma_{or} = M\frac{G_{Al}b}{\pi\sqrt{(1-\nu)}}\frac{\ln\left(\frac{2R}{b}\right)}{\lambda_{e-e}} \qquad (8)$$

where the mean planar radius[64] is given by $R = \frac{\pi}{4}\langle R \rangle$, $\nu = 0.354$ is the Poisson's ratio for Al[47], and the inter-precipitate distance[64] $\lambda_{e-e} = \left(\sqrt{\frac{2\pi}{3\phi}} - \frac{\pi}{2}\right)\langle R \rangle$.

Coherency strengthening, $\Delta\sigma_{cs}$, can be estimated using [46,65,63]:

$$\Delta\sigma_{cs} = M\chi(\epsilon G_{Al})^{3/2}\left(\frac{\langle R \rangle \phi b}{\Gamma}\right)^{1/2} \qquad (9)$$

where $\chi = 2.6$ for fcc metals[64], ϵ is the mismatch parameter approximated by $\frac{2}{3}\delta$; $\delta = 1.23\%$ and 0.75% are taken as the lattice parameter mismatches for the $Al_{3-x}Zn_xNi$ and $Al_{3-x}Zn_xZr$ precipitates estimated from the composition-dependent lattice parameter[12,13,65,66], and $\Gamma = \frac{1}{2}G_{Al}b^2$ is the line tension of dislocations in Al.

Generally, precipitation hardening is governed by either dislocation by-pass (Orowan-type) or dislocation shearing mechanisms. At peak strength, only the shearing mechanism was considered and the contributing factors in this mechanism are coherency strengthening ($\Delta\sigma_{cs}$), modulus mismatch strengthening ($\Delta\sigma_{ms}$), and order strengthening ($\Delta\sigma_{or}$) [46,63]. Regardless of the unavailability of exact data and approximations made for some of the parameters used in the equations above, these models successfully predicted the maximum yield strength observed experimentally. Using equations 4-7 and the data in Table 5, the contribution of each strengthening mechanism to the yield strength of 1.7Zn0.07Zr was estimated as $\Delta\sigma_{or} \approx 148\,MPa$, $\Delta\sigma_{os} \approx 114\,MPa$, $\Delta\sigma_{cs} \approx 18\,MPa$ and $\Delta\sigma_{ms} \approx 118\,MPa$ for Orowan, order, coherency strain, and modulus mismatch strengthening, respectively. The larger value between $\Delta\sigma_{cs} + \Delta\sigma_{ms}$ ($\sim 136\,MPa$) and $\Delta\sigma_{os}$ ($\sim 114\,MPa$) determines the resultant yield strength increment due to the shearing mechanism[46,63]. As a result, the yield strength ($\Delta\sigma_{ppt}$) of 1.7Zn0.07Zr at 450 ℃, due to precipitation hardening, was estimated as $136\,MPa$ from $\Delta\sigma_{cs} + \Delta\sigma_{ms}$ (ignoring Orowan strengthening). Therefore, the significant difference between the estimated and measured yield strength of 1.7Zn0.07Zr is 20 MPa, which could be attributed to the solid solution strengthening (not considered in the estimate) from the remaining Zn in the matrix. The difference between estimated and measured strength values could also be a result of some of the approximated parameters used in the estimation, due to a lack of exact theoretical or experimental data for the $Al_{3-x}Zn_xZr$ precipitate.

Table 5. Measured precipitate mean radii,$\langle R\rangle$, of $L1_2$ precipitates located at the dendritic centers of 1.8Zn0.05Ni and 1.7Zn0.07Zr, after isochronal aging at 250 and 450 ℃, respectively.

Specimen	Aging Temperature ℃	Mean precipitate radius $\langle R\rangle\ nm$	Number of counted precipitates
1.8Zn0.05Ni	250	4.0	285
1.7Zn0.07Zr	450	2.5	201

Similar to the estimation made for the 1.7Zn0.07Zr alloy, the yield strength due to precipitation ($\Delta\sigma_{ppt}$) of the 1.8Zn0.05Ni alloy at peak strength was estimated as 108 MPa from $\Delta\sigma_{cs} + \Delta\sigma_{ms}$. The measured peak strength for this specimen was 125 MPa. The observed difference between the estimated and measured strength values is 17 MPa, which could also be attributed to the solid solution strengthening due to the remaining Zn left in the matrix and the gross approximation made for some of the parameters used.

6. Conclusions

When the solubility limits of the solutes in Al are not considered and all the solute atoms are assumed to remain in solid solution (no precipitation), the electrical conductivity predictions from DFT simulations agree well with experiment (expt-SS). According to Figure 5, the addition of Zn to binary Al-TM alloys only slightly reduced the electrical conductivity. This demonstrates

that Zn has a minimal impact on electrical conductivity when in- and out-of solid solution. The experimental electrical conductivity data in Figures 10 and 11 show that at equivalent atomic percentages of alloying elements, Al-Zn-Ni has a higher electrical conductivity than Al-Zn-Zr, as predicted by DFT.

Using enthalpy of formation, the predicted zero-temperature stabilities of Al-Zn-Ni and Al-Zn-Zr precipitate phase structures revealed the equilibrium crystal structures of Al_3Ni and Al_3Zr as $D0_{11}$ and $D0_{23}$, respectively. The step-by-step inclusion of Zn into the precipitate phase demonstrated that the resulting $Al_{3-x}Zn_xNi$ and $Al_{3-x}Zn_xZr$ precipitates have stable $L1_2$ structures, which was confirmed by experiment. These simulations were performed at 0 K, hence, the influence of temperature on the stability of the $L1_2$ structures was not computationally determined in this study.

Heat treatment experiments showed that the difference in peak microhardness temperatures of Al-Zn-Ni and Al-Zn-Zr alloys is due to the difference in nucleation and growth rates of Ni and Zr precipitates in aluminum. Peak microhardness values of both alloys increase with Zn loading, whereas conductivity drops slightly. This study also showed that an increase in electrical conductivity of Al-Zn-Zr was achieved at peak strength due to precipitation of the solute atoms from matrix, although this was not observed in the Al-Zn-Ni samples due to the much smaller impact of Ni on conductivity.

A microstructural study of Al-Zn-Ni revealed that for alloys with a lower Zn composition (0.5Zn0.05Ni and 1.0Zn0.05Ni), the precipitates retained their orthorhombic $D0_{11}$-Al_3Ni structure, because there were little or no Zn atoms in their precipitate phases. For higher Zn compositions, the precipitate morphology transformed to a spheroidal-$L1_2$ $Al_{3-x}Zn_xNi$ structure as shown in Figure 12c,f. This indicates that the inclusion of Zn is likely responsible for the $D0_{11} \rightarrow L1_2$ precipitate transformation. Since Al_3Zr already has a metastable $L1_2$ structure during aging, there was no precipitate transformation required at 450 ℃. The crystal structure of $Al_{3-x}Zn_xZr$ precipitates formed in 1.7Zn0.07Zr remained as $L1_2$. Thus, the addition of Zn into the Al_3Zr precipitate phase did not alter the $L1_2$ phase structure.

In summary, these alloys have demonstrated a good balance between electrical conductivity and microhardness, relative to several other electrical conductors used for high conducting applications. Examples of such alloys are 1350 aluminum alloy (AA) and Al-Mg-Si (AA6101) commonly used as electrical conductors for overhead power lines. The laboratory fabricated AA1350 has high electrical conductivity (35.7 MS/m) but very low ultimate tensile strength, while Al-Mg-Si (AA6101) has a very high strength but lower electrical conductivity, depending on the amount of Mg_2Si solute present[67,68].

Acknowledgements

This research was funded by the NSF I/UCRC on Novel High Voltage/Temperature Materials and Structures (Grant IIP-1362040). SUPERIOR, a high-performance computing cluster at Michigan Technological University, was used in obtaining DFT simulation results presented in this publication. NSF MRI fund (Grant #1429232) was used to set up the S-TEM facility used to acquire all the microscopy data included in this study.

References

[1] J. Allison, *Integrated computational Materials Engineering: a perspective on progress and Future steps*, Enabling ICME, JOM, 63 (2011) 15-18.

[2] D.S. Sholl and J. A. Steckel, *Density Functional Theory. A Practical Introduction*, A John Wiley and Sons, Inc, Publication, (2009).

[3] P.J. Hasnip1, K. Refson, M.I.J. Probert, J.R. Yates, S.J. Clark, C.J. Pickard, *Density functional theory in the solid state*, Royal Society Publishing, (2014).

[4] D. Shi, B. Wen, R. Melnik, S. Yao, T. Li, *First-Principles Studies of Al-Ni Intermetallic Compounds*, Journal of solid State Chemistry, (2009) 2664-2669.

[5] G. Ghosh, M. Asta, *First Principle Calculations of Structural Energetics of Al-TM (TM = Ti, Zr, Hf) Intermetallics*, Acta Materialia, 53 (2005) 3225-3252.

[6] J. Wang, S.L. Shang, Y. Wang, Z.G. Mei, Y.F. Liang, Y. Du, Z.K. Liu, *First Principle Calculations of Binary Al Compounds: Enthalpy of Formation and Elastic Properties, CALPHAD: Computer Coupling of Phase Diagrams and Thermochemistry*, 35 (2011) 562-573.

[7] X.L. Yuan, D.Q. Wei, X.R. Chen, Q.M. Zhang, Z.Z. Gong, *The First Principles Calculations for the Elastic Properties of Zr_2Al under Compression*, Journal of Alloys and Compounds 509 (2011) 769-774.

[8] F.Z. Chrifi-Alaoui, M. Nassik, K. Mahdouk, J.C.Gachon, *Enthalpies of Formation of the Al-Ni Intermetallic Compounds*, Journal of Alloys and Compounds, 364 (2004) 121-126.

[9] G. Ghosh, A. van de Walle, M. Astra, *First Principles Phase Stability Calculations of Pseudobinary Alloys of $(Al,Zn)_3Ti$ with $L1_2$, $D0_{22}$ and $D0_{23}$ Structures*.

[10] J.E. Hatch, *Aluminum: Properties and Physical Metallurgy*, American Society for Metals, (1984).

[11] K. Knipling, D. Dunand, D. Seidman, *Criteria for developing castable creep resistant aluminum-based alloys- A review*, Basic (2006) 246-265.

[12] K.E. Kniplng, D.C. Dunand, D.N. Seidman, *Precipitation evolution in Al-Zr and Al-Zr-Ti alloys during aging at 450* ℃ *compared to 600* ℃, Acta Materialia 58 (2008) 1182–1195.

[13] K.E. Knipling, D.C. Dunand, D.N.Seidman, *Precipitation evolution in Al-Zr and Al-Zr-Ti alloys during isothermal aging at 375 – 425* ℃, Acta Materialia 56 (2008) 114 – 127.

[14] G Cubiotti, E E Krasovskii, O V Slobodyan, Yu N Kucherenko and V Antonov, *The electronic structure of Al_3Ni*, Journal of Physics: Condensed Matter, Volume 7, Number 25.

[15] M.E. Fine, G. Ghosh, D. Isheim , S. Vaynman, K. Knipling, J.Z. Liu, *Alloy Design of Nanoscale Precipitation Strenghtened Alloys: Design of Heat Treatable Aluminum Alloy Useful to 400 °C*, Final Report for Department of Energy (2006).

[16] A.E. Carlsson and P.J.Meschter, J. Mater. Res. 4, 1060 (1989).

[17] D.M. Nicholson, G.M. Stocks, W.M. Temmerman, P. Sterne and D.G. Pettifor, *High-Temperature ordered intermetallix alloys III*, C.T. Liu, A.I. Taub, N.S. Stoloff and C.C. Koch (eds.), 17, MRS, Pittsburgh, PA (1989).

[18] S. Zhang, J.P. Nic and D.E. Mikkola, *New cubic phases formed by alloying Al_3Ti with Mn and Cr*, Scripta Metallurgica, 24 (1990) 57–62.

[19] G. Kresse, M. Marsman and J. Furthmuller, *Vienna Ab-initio Simulation Package, VASP the Guide*, Computational Materials Physics, Faculty of Physics, University of Wien, Sensengasse 8/12, A-1090 Wien, Austria (2014).

[20] R. Kubo, J. Phys. Soc. Jpn. 12, (1957) 570.

[21] D.A. Greenwood, Proc. Phys. Soc., 71, (1958) 585.

[22] G.K.H. Madsen and D.J. Singh, *BoltzTraP. A code for calculating band-structure dependent quantities*, Computer Physics Communications, (2006) 175(1): p. 67-71.

[23] D.S. Sholl and J.A. Steckel, Density functional theory: A practical introduction, A John Wiley and Sons, Inc., Publication (2009)

[24] A.R. Shojaei, *Electrical conductivity plus probability of superconductivity in a-CuSe/klockmannite; bulk and nano-layers*, *Journal of Alloys and Compounds*, 632 (2015) 568-574.

[25] A.H., S.A. Khan, and S. Auluck, *Thermoelectric properties of a single graphene sheet and its derivatives*, Journal of Materials Chemistry C, (2014) 2(13): p. 2346-2352.

[26] A.H. Reshak and S. Auluck, *Thermoelectric properties of Nowotny-Juza NaZnX (X = P, As and Sb) compounds*, Computational Materials Science, (2015) 96: p. 90-95.

[27] A.H. Reshak, *$Fe_2MnSi_xGe_{1-x}$: influence thermoelectric properties of varying the germanium content*, Rsc Advances, (2014) 4(74): p. 39565-39571.

[28] H. Pal, S. Kumar, M. De, *Microstructure and mechanical property of α-Al-Zn-Cu alloys aged at room temperature*, Materials Transactions, JIM, 36:4 (1995) 490–495.

[29] G. Ghosh, A. Van De Walle, M. Asta, *First-principles phase stability calculations of $L1_2$, $D0_{22}$ and $D0_{23}$ structures in Al-TM(=Ti,Zr,Hf)-Zn systems*, Proceedings of an International Conference on Solid-Solid Phase Transformations in Inorganic Materials, Vol 2, (2005) 651-656.

[30] K.E. Knipling, R.A. Karnesky, C.P. Lee, D.C. Dunand, D.N. Seidman, *Precipitation evolution in Al-0.1Sc, Al-0.1Zr and Al-0.1Sc-0.1Zr (at. %) alloy during isochronal aging*, Acta Materialia 58 (2010) 5184–5195.

[31] T. Marumo, S. Fujikawa, K. Hirano: J. Japan Inst. Light Metals 23 (1973) 17–25.

[32] S.I. Fujikawa, Defect diffusion forum, (1997) 143–147:115–20

[33] S. Dias, R. Messer, A. Seeger: Mater. Sci. Forum 15 – 18 (1987) 419.

[34] G. Erdelyi, D.L. Beke, F.J. Kedves, I. Godeny: Phil. Mag. B 38 (1978) 445.

[35] N.L. Peterson, S.J. Rothman: Phys. Rev. B 1 (1970) 3264.

[36] T. Marumo, S. Fujikawa, K. Hirano: J. Japan Inst. Light Metals 23 (1873) 17.

[37] T. Marumo, S. Fujikawa, K. Hirano: J. Japan Inst. Light Metals 23 (1873) 17.

[38] T. Gladman, *Precipitation hardening in metals*, Materials Science and Technology, (1999) 15:1, 30-36.

[39] T.R. Prabhu, *Effect of ageing time on the mechanical and conducting properties of various round bar diameters of AA 2219 Al alloy*, Engineering Science and Technology, an International Journal 20 (2017) 133–142.

[40] A.S. Wadhwa, H.S. Dhaliwal, *A Textbook of Engineering Material and Metallurgy*, Laxmi Publications, (2008) 316.

[41] V. Raghavan, *Section II: Phase diagram evaluations, Al-C-Co (Aluminum-Carbon-Cobalt)*, ASM International, (2008) 29:46 – 48.

[42] [2017b] Thermo-Calc Software TCAL5: Al-Alloys v5.0 database (accessed 16 January, 2018)

[43] C. Wang, Qiang Wanga, Z. Wang, H. Li, K. Nakajima, J. He, *Phase alignment and crystal orientation of Al_3Ni in Al–Ni alloy by imposition of a uniform high magnetic field*, Journal of Crystal Growth 310 (2008) 1256–1263.

[44] D.N. Seiman, E.A. Marquis, D.C. Dunand, *Precipitation strengthening at ambient and elevated temperatures of heat treatable Al(Sc) alloys*, Acta Materialia 50 (2002) 4021–4035.

[45] D. Tabor, Br J Appl Phys (1956); 7: 159-66

[46] Z.G. Wang, W. Zhou, L.M. Fu, J.F. Wang, R.C. Luo, X.C. Han, B. Chen, X.D. Wang, *Effect of coherent $L1_2$ nanoprecipitates on the tensile behavior of a fcc-based high-entropy alloy*, Materials Science and Engineering A 696 (2017) 503-510

[47] M.A. Meyers, K.K. Chawla, *Mechanical metallurgy: principles and applications*. NJ: Prentice-Hall; (1984).

[48] R. Gaillac, P. Pullumbi and F. X. Coudert, http://progs.coudert.name/elate/mp?query=mp-622209, *J. Phys. Condens. Matter*, 2016, 28, 275201

[49] L. Fu, Jiang-Ling Ke, Q. Zhang, Bi-Yu Tang, Li-Ming Peng, and Wen-Jiang Ding, *Mechanical properties of $L1_2$ type Al_3X (X = Mg, Sc, Zr) from first-principles study*, Phys. Status Solidi B, (2012) 1-7.

[50] W. Na and T. Bi-Yu, *Structural, elastic and electronic properties of $L1_2$ aluminum phases from first principles calculation*, Acta Phys. Sin., 58 (2009), 230–234.

[51] Z. Wei, S. Tou, B. Wu, K. Bai, *First principle investigation of crystal lattice structure, thermodynamics and mechanical properties in $ZnZrAl_2$ intermetallic compound*, Solid State Communications 247 (2016)82–87

[52] O. Fadayomi, P. Sanders and G. Odegard, *Microstructures and properties of precipitation hardened 0.25Zr and 3.6Zn0.25Zr (wt.%) alloys at 450 and 600 °C*, submitted to Journal of Alloys and Compounds (2018).

[53] A.J. Ardell, *Ch 12: Intermetallics as precipitates and dispersoids in high-strength alloys*. In: Westbrook JH, Fleischer RL, editors. Intermetallic compounds: principles and practice, vol. 2. Chichester: John Wiley & Sons; (1994) 257.

[54] H.J. Frost, M.F. Ashby, *Deformation-mechanism maps: the plasticity and creep of metals and ceramics*. New York: Pergamon Press (1982).

[55] Y. Fan and M.M. Makhlouf, *The Al-Al_3Ni Eutectic Reaction: Crystallography and Mechanism of Formation*, Metallurgical and Materials Transactions A, (2015) 46A: 3808–3812.

[56] P.H.L. Souza, C.A.S. de Oliveira, J.M.V. Quaresma, *Precipitation hardening in dilute Al-Zr alloys*, J Mater Res Technol. 2018; 7(1): 66–72.

[57] W. Lefebvre, et al., *Tracking the path of dislocations across ordered Al_3Zr nano-precipitates in three dimensions.* Scripta Materialia, (2014) 70: p. 43- 46

[58] R. Hyland, et al., *Al (fcc): Al_3Sc ($L1_2$) interphase boundary energy calculations*, Acta materialia, (1998) 46(10): p. 3667-3678.

[59] M.A. Phillips, B.M. Clemens, and W.D. Nix, *A model for dislocation behavior during deformation of Al/Al_3Sc (fcc/$L1_2$) metallic multilayers.* Acta Materialia, (2003) 51(11): p. 3157-3170.

[60] X. Gao, J. Wang, X. Wu, R. Wang and Z. Jia, *Effects of Alloying Atoms on Antiphase Boundary Energy and Yield Stress Anomaly of $L1_2$ Intermetallics: First-Principles Study*, Crystals (2018) 8, 96.

[61] T. Hong and A.J. Freeman, *Effect of antiphase boundaries on the electronic structure and bonding character of intermetallic systems: NiAl*, Physical Review, 43 (1991) 8.

[62] O. I. Gorbatov, et at., *Effect of composition on antiphase boundary energy in Ni_3Al based alloys: Ab initio calculations*, Physical Review B, 93, 224106 (2016).

[63] K.E. Knipling, R.A. Karnesky, C.P. Lee, D.C. Dunand, D.N. Seidman, *Precipitation evolution in Al-0.1Sc, Al-0.1Zr and Al-0.1Sc-0.1Zr (at.%) alloy during isochronal aging*, Acta Materialia 58 (2010) 5184–5195.

[64] A.J. Ardell, Metallurgical Transactions A: *Precipitation hardening*, Volume 16, Issue 12, (1985) 2131–2165.

[65] G Cubiotti *et al. J. Phys.: Condens. Matter* 7 (1995) 4865

[66] C.B. Fuller, D.N. Seidman and D.C. Dunand, *Mechanical properties of Al(Sc,Zr) alloys at ambient and elevated temperatures*, Acta Materialia 51 (2003) 4803–4814.

[67] A.K. Guptaa, D.J. Lloyda, S.A. Court, *Precipitation hardening in Al–Mg–Si alloys with and without excess Si*, Materials Science and Engineering: A, 316 (2001) 11-17.

[68] X. Sauvage, E.V. Bobruk, M. Yu.Murashkin, Y. Nasedkina, N.A. Enikeev, R.Z. Valiev, *Optimization of electrical conductivity and strength combination by structure design at the nanoscale in Al–Mg–Si alloys*, Acta Materialia, 98 (2015) 355-366.